FISEVIER

Contents lists available at ScienceDirect

Materials and Design

journal homepage: www.elsevier.com/locate/matdes



High-throughput synthesis of Mo-Nb-Ta-W high-entropy alloys via additive manufacturing



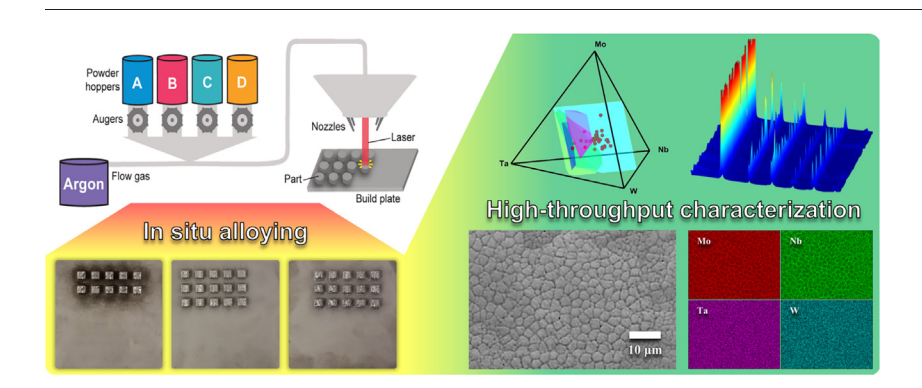
Michael Moorehead ^{a,*}, Kaila Bertsch ^{b,c}, Michael Niezgoda ^b, Calvin Parkin ^a, Mohamed Elbakhshwan ^a, Kumar Sridharan ^{a,b}, Chuan Zhang ^d, Dan Thoma ^{a,b,c}, Adrien Couet ^{a,b}

- ^a University of Wisconsin-Madison, Engineering Physics Dept., Madison, WI 53706, USA
- ^b University of Wisconsin-Madison, Materials Science & Engineering Dept., Madison, WI 53706, USA
- ^c University of Wisconsin-Madison, Grainger Institute for Engineering, Madison, WI 53706, USA
- ^d Computherm LLC, Middleton, WI 53562, USA

HIGHLIGHTS

- A high-throughput bulk materials synthesis technique was developed.
- HEA sample arrays were produced via in situ alloying of elemental powders.
- HEA samples were homogeneous and single-phase disordered BCC.
- SEM, EDS, and XRD was performed while samples remained on build plate.
- CALPHAD modeling was used to map the Mo-Nb-Ta-W composition space.

GRAPHICAL ABSTRACT



ARTICLE INFO

Article history: Received 20 August 2019 Received in revised form 17 October 2019 Accepted 12 November 2019 Available online 14 November 2019

Keywords:
High-entropy alloy
MoNbTaW
Additive manufacturing
High throughput
In situ alloying

ABSTRACT

High-entropy alloys (HEAs) are a class of alloys that can exhibit promising properties including enhanced irradiation resistance, high-temperature strength, and corrosion resistance. However, they exist in a relatively unexplored region of quasi-limitless composition space. Thus, to enable the development of promising compositionally complex alloys, such as HEAs, high-throughput methods are needed. Such high-throughput capabilities are developed and presented in this work. In situ alloying through additive manufacturing was employed to produce arrays of different HEA compositions. Sample arrays were then characterized by scanning electron microscopy (SEM), energy-dispersive X-ray spectroscopy (EDS), and X-ray diffraction (XRD), all while remaining on the build plate. The top surface of each sample was compositionally homogeneous, as determined by EDS, and each sample exhibited a single-phase, disordered crystal structure, as determined by XRD. CALculation of PHAse Diagrams (CALPHAD) modeling was used to determine the equilibrium phases of each HEA composition at lower temperatures, the results of which were compared with XRD results. Implications of high-throughput synthesis techniques and the coupling of high-throughput characterization and modeling techniques are discussed in the context of alloy development.

© 2019 The Authors. Published by Elsevier Ltd. This is an open access article under the CC BY license (http://creativecommons.org/licenses/by/4.0/).

^{*} Corresponding author at: 1500 Engineering Dr. ERB 927, Madison, WI 53706, USA.

E-mail address: moorehead2@wisc.edu (M. Moorehead).

1. Introduction and motivation

Unlike conventional alloys, which typically comprise a single primary element with minor alloying elements added to modify the properties, HEAs are composed of multiple principle elements often in nearequimolar ratios. An alloy is commonly considered to be an HEA if it has multiple principle elements present in concentrations between 5 at.% and 35 at.% [1]. Beyond novelty, HEAs have gained interest for their promising properties including enhanced irradiation resistance [2], high-temperature strength [3], and corrosion resistance [4]. Individual HEAs have previously been synthesized using arc melting [5], spark plasma sintering (SPS) [6], mechanical alloying (MA) [7], and physical vapor deposition (PVD) [8], among other classical metallurgical techniques. However, the vast space of possible compositional variants under the HEA definition makes synthesis, characterization, modeling, and optimization of HEA compositions impractical using conventional methods. Development of accelerated, high-throughput techniques for the production and screening of novel alloys, such as HEAs, is thereby necessary if the development of compositionally complex alloys is to progress efficiently.

To date, most high-throughput alloy synthesis techniques rely on producing compositional gradients to form a range of alloy compositions, as is the case for diffusion multiples [9,10], combinatorial thin films [11–14], additively manufactured gradients [15–17], combustion synthesis [18], and in situ nanotip melting [19]. Inherently, this limits the usability of these materials for materials testing and characterization since a single composition of interest typically only exists in a vanishingly thin 1D line or 2D plane. Moreover, the chemically graded structures are thermodynamically unstable which minimizes their utility for testing at elevated temperatures where diffusion is no longer negligible. More recent work has sought to produce arrays of discrete material compositions by depositing varying amounts of a single elemental powder onto a metallic substrate and alloying the powder into the substrate by laser melting [20], however, such techniques are limited to producing patches of alloyed material at the surface of the substrate whose compositions cannot be varied independently from the substrate material. Consequently, the need exists for high-throughput synthesis techniques capable of producing bulk (3D) samples of freely chosen compositions, with microstructures that more closely resemble that of industrial materials.

Using HEAs as a venue for developing such high-throughput techniques, this work seeks to extend high-throughput materials synthesis to bulk materials such that it may be coupled with existing high-throughput characterization and modeling techniques. Specifically, implementation of additive manufacturing and the further development of in situ alloying techniques have enabled the *printing* of different HEA compositions, in 3D-component arrays, on a single build plate. The printing of such arrays on a single plate has enabled the use of high-throughput microstructural characterization techniques, the results of which will be presented herein, in addition to enabling future high-throughput testing of compositional arrays.

2. Methods and materials

To rapidly produce arrays of different HEA compositions, additive manufacturing in the form of directed energy deposition (DED) was performed using an Optomec LENS MR-7, schematically represented in Fig. 1. The LENS MR-7 is a powder-based metals 3D printer operating in a closed chamber filled with argon and fed by four independently controlled powder hoppers. Powders from each hopper are drawn into a gas line of flowing argon by the rotation of an auger located at the base of each hopper. These powders are aggregated in a central gas line and consequently mixed by the turbulent gas flow during transit to the printhead. At the printhead, the mixed powder is sprayed out by four nozzles, with rotational symmetry about the optic axis of the printhead, where it encounters a laser impinging on the surface of the

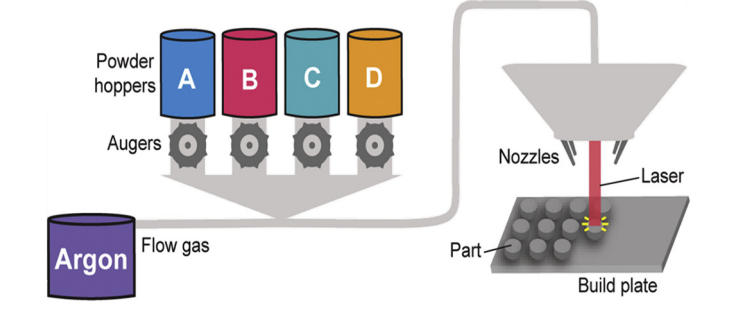


Fig. 1. Schematic illustration of the LENS MR-7 system used in this study.

build plate. The laser, with an approximate spot size of $600 \, \mu m$ and focal point ~380 μm below the surface, forms a melt pool on the surface of the build plate where incoming powder heated by the laser becomes incorporated. This melt pool can then be dragged across the surface of the build plate, by moving the stage it is affixed to, leaving behind solidified material in its wake. A continuous solid/liquid interface is maintained as the laser moves along the build path, and cooling rates in excess of $10^3 \, \text{K/s}$ can be obtained in 3D geometries [21]. By steering the path of the laser across the surface of the build plate through stage movements, material can be deposited in arbitrary geometries.

For this research, hoppers in the LENS MR-7 were each filled with a single elemental powder, either Mo, Nb, Ta, or W. These elements were selected to produce compositions near that of the four-component equimolar HEA MoNbTaW, which has been previously shown to form a single-phase solid solution [22,23]. Furthermore, this alloy is predicted to be stable over a broad temperature range [24,25], reducing the likelihood of phase transformations, which can cause changes in geometry and additional stresses in the printed part. Additionally, by maintaining separation of elemental powders prior to printing, access to any linear combination of the four elements is achievable.

Plasma spheroidized Mo, Nb, Ta, and W powders, each in the size range of ~45 μm –150 μm (-100/+325 mesh), were procured from the company HC Starck and the morphology and size distribution can be seen in Fig. 2. While broad size ranges of powders and the presence of irregularly shaped powders have been linked to defects, including lack-of-fusion porosity, in additively manufactured parts using powder-bed techniques [26,27], it is still unclear that this relationship applies to parts manufactured through DED techniques, which feature blown powder, higher laser powers, and slower scan speeds. For this work, the size range of powders recommended by the LENS manufacturer was used to ensure proper functioning of the powder handling components.

Nominal dimensions of the printed parts were 6.35×6.35 × 3.175 mm, comprised of five print layers each with a hatch spacing of 0.381 mm; the hatch pattern was rotated 60° between each layer. The Z step size was 0.254 mm, however in practice the deposited layer height was approximately twice this, depending on composition. To ensure sufficient homogeneity, after the final deposition pass, a remelting pass was performed whereby the laser was rastered across the sample surface without being fed powders from the hoppers. Deposition passes were performed with a laser power of 800 W and a scan speed of 25.4 cm/min and remelting passes were performed with a laser power of 1000 W and a scan speed of 177.8 cm/min. The increased scan speed was found to be necessary to avoid high back reflection from the laser. The total time required to set the composition of, print, and remelt a single sample stub was <5 min. All samples stubs were printed onto 316 stainless steel build plates (100 \times 100 \times 6.35 mm). The argon atmosphere was sampled continuously throughout each printing campaign, and the measured oxygen concentration was reduced to <10 ppm before printing. However, after the onset of printing, the measured oxygen concentration quickly dropped to <1 ppm, due to oxygen

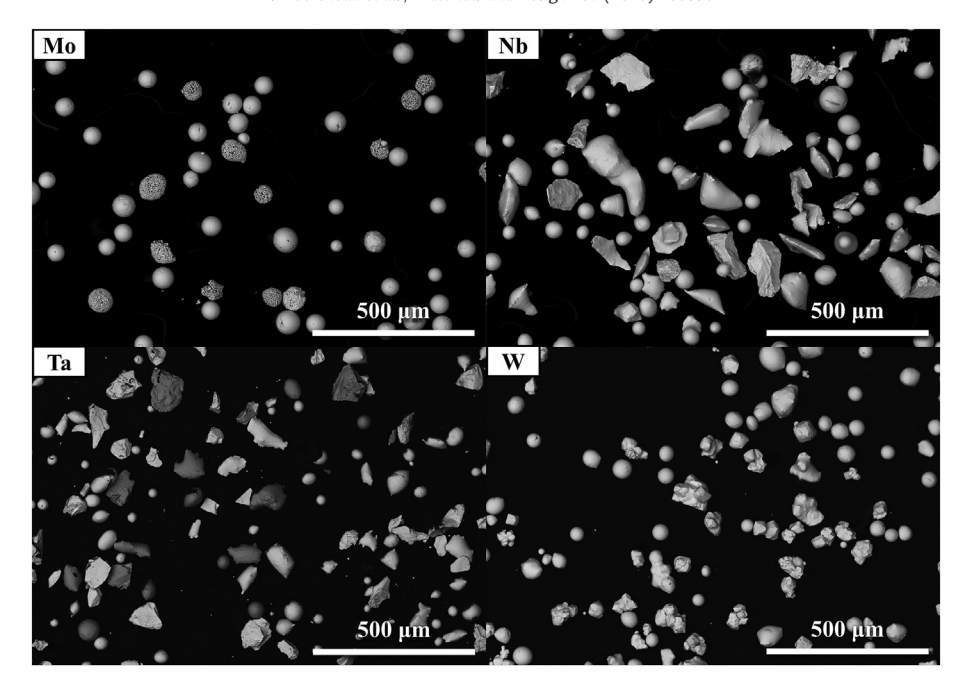


Fig. 2. Backscatter SEM images of Mo, Nb, Ta, and W powders used in this study, sourced from HC Starck.

gettering by the printed material, and remained at this level for the duration of each printing campaign.

In this work, calibrations were performed to measure the mass flow rate of each elemental powder as a function of auger RPM for their respective hoppers, the results of which were used in final build composition predictions. Three printing iterations producing a total of 40 sample stubs were performed. 31 samples are included in the analysis hereinafter as the remaining samples were produced as part of other parameter optimization experiments. In each iteration, all printing parameters were kept constant except the powder hopper RPM, which was varied to produce different compositions while maintaining a total atomic flow rate of ~0.1 mol/min (~12–15 g/min) for each composition.

Arrays of printed samples were imaged using a JEOL JSM-6610 scanning electron microscope (SEM) at the Wisconsin Nanoscale Imaging and Analysis Center, equipped with energy-dispersive X-ray spectroscopy (EDS) for chemical analysis. Phase identification was performed using X-ray diffraction (XRD) with a Bruker D8 Discover. Lattice parameters were calculated from extrapolation of the Nelson-Riley function using collected XRD data [28]. All initial microstructural characterization (XRD, SEM, EDS, etc.) was performed non-destructively without removing samples from the build plate. After initial characterization, 2–3 samples from each build plate were removed and polished for more in-depth microstructural and chemical analysis using SEM and EDS.

For comparison of the additively manufactured microstructure with that of conventional metallurgy, a ~50-g ingot of the equimolar MoNbTaW HEA was cast using an Arcast Arc200 arc melter. Precursor materials were elemental foils of Mo and Ta, small billets of Nb, and W wire, all >99.9% in purity. The cast ingot was flipped and remelted multiple times to ensure macroscopic chemical homogeneity.

In addition to experimental work, high-throughput computational methods were employed to assess the phase stability of the HEA compositions produced via additive manufacturing. The CALPHAD (CALculation of PHAse Diagrams) approach was chosen for its relative accuracy and computational efficiency in calculating equilibrium phases by applying an energy-minimization procedure to large thermodynamic databases of Gibbs energies, as a function of temperature, pressure, and composition [29,30]. Specifically, the computation software, PanDat™ [31], equipped with a high-throughput calculation (HTC) tool, was used to develop quaternary phase diagrams in the Mo-Nb-Ta-W composition space.

3. Results

For reference, pictures of the build plates from each printing iteration are shown in Fig. 3. The top surfaces of the printed sample stubs were found to be wavy, but smooth and reflective suggesting minimal oxidation has occurred during synthesis. The height variation within a

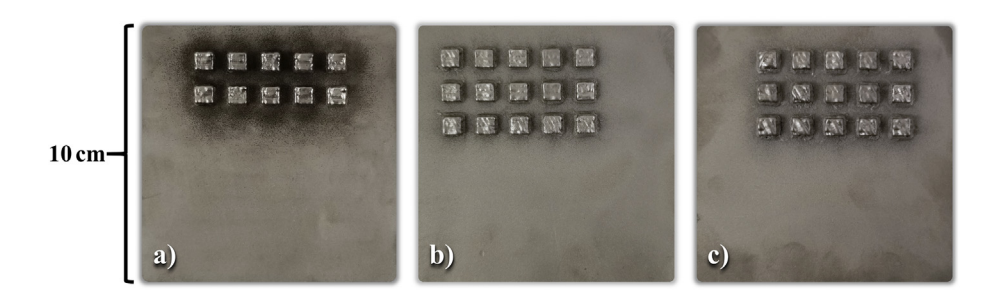


Fig. 3. Build plates featuring Mo-Nb-Ta-W arrays from the a) first, b) second, and c) third printing iterations. Note: for clarity, build plates from the second and third iterations were sand blasted before imaging.

single stub is not thought to be substantial enough to impact chemical or crystallographic measurements by energy-dispersive spectroscopy (EDS) or X-ray diffraction (XRD), however samples would likely need to be mirror polished for meaningful further irradiation, corrosion, and mechanical testing.

3.1. Compositional predictions

One challenge of alloying elemental powders in situ is controlling the final composition of the built part. The difficulty is that several variables such as elemental vapor pressure, powder geometry, powder reflectivity, elemental mixing enthalpies, etc. can affect how the powders absorb energy from the laser and how much of the material enters the melt pool and mixes. The result is that often the composition of the powder exiting the nozzles of the 3D printer is not necessarily the composition of the final part. As such, multiple iterations of printing and prediction refinement were necessary to narrow the gap between actual compositions (measured from EDS line scans across the sample surface) and predicted compositions, the results of which are shown in Fig. 4.

3.1.1. First iteration

The predicted compositions for the first printing iteration were based solely on the mass flow rate versus powder hopper RPM calibrations, performed separately for each element. The result of each powder calibration experiment is a relationship shown by Eq. (1).

$$m_i = \alpha_i * (RPM)_i + \beta_i \tag{1}$$

Here, m_i is the mass flow rate of element i which is related to the RPM selected for that powder hopper by experimentally determined coefficients α_i and β_i . While a non-zero value for β_i would not seem intuitive (as this would imply a non-zero mass flow rate while the powder hopper is idle), most of the elements studied had value for β_i whose magnitude was non-negligible. Possible reasons for this include a potential minimum RPM for the stepper motor which would be necessary for smooth, continuous auger rotation. From the mass flow rate measurements, the mass fraction, w_i , of species i in the incoming powder is simply the ratio of the mass flow rate of species i over the total mass flow rate as shown in Eq. (2).

$$w_i = \frac{m_i}{\sum_{i=1}^n m_i} = \frac{\alpha_i * (RPM)_i + \beta_i}{\sum_{i=1}^n \left[\alpha_i * (RPM)_i + \beta_i\right]} \tag{2}$$

Similarly, from Eq. (2), using M_i as the molar mass, the atomic fraction, x_i , of species i can be written as shown in Eq. (3).

$$x_i = \frac{M_i * m_i}{\sum_{i=1}^n M_i * m_i} = \frac{M_i * \left[\alpha_i * (RPM)_i + \beta_i\right]}{\sum_{i=1}^n M_i * \left[\alpha_i * (RPM)_i + \beta_i\right]} \tag{3}$$

For the first printing iteration, compositions near the equimolar MoNbTaW composition were explored by varying the powder hopper RPMs using Eq. (1). These measured sample compositions were compared retroactively to the compositions predicted using Eq. (3) and are shown in Fig. 4a. Here it can be seen that the actual sample compositions are greatly depleted in Mo and enriched in Nb and W compared to the predictions. While likely caused by several phenomena occurring in concert, previous studies have observed similar trends with Mo and Nb, which were attributed to the relatively high vapor pressure of Mo leading to volatilization as well as the relatively low melting point of Nb leading to preferential melting [32]. The enrichment of W, however, is not easily explained by trends in melting point or vapor pressure and may instead be a result of other extrinsic characteristics of the W powder, such as the morphology or reflectivity, though this remains speculative at this point.

3.1.2. Second iteration

Rather than mounting a bottom-up campaign to determine the powder and system characteristics that give rise to the discrepancies between the predicted and measured sample stub compositions, a top-down approach was taken by lumping all of the effects into a single fitting term, R, dubbed the *retention rate*. Using this fitting parameter, the predicted atomic fraction of each element in the printed material can be written as shown in Eq. (4).

$$x_i = \frac{R_i * M_i * m_i}{\sum_{i=1}^n R_i * M_i * m_i} = \frac{R_i * M_i * \left[\alpha_i * (RPM)_i + \beta_i\right]}{\sum_{i=1}^n R_i * M_i * \left[\alpha_i * (RPM)_i + \beta_i\right]}; where \ 0 \le R_i \le 1$$

The retention rate for each element was then calculated by performing a least-squares fit on Eq. (4) using the measured compositions from the first printing iteration, α_i and β_i values from the mass flow rate calibration experiments, and input RPMs.

For the second iteration, all possible compositions of the $A_{20}B_{30}C_{20}D_{30}$ type (e.g. $Mo_{20}Nb_{30}Ta_{20}W_{30}$, $Mo_{30}Nb_{30}Ta_{20}W_{20}$, etc.), the $A_{20}B_{20}C_{20}D_{40}$ type (e.g. $Mo_{20}Nb_{20}Ta_{20}W_{40}$, $Mo_{20}Nb_{40}Ta_{20}W_{20}$, etc.), and the equimolar composition were targeted. Using R_i values calculated from applying Eq. (4) to the data from the first printing iteration, the RPMs necessary to achieve these final compositions were

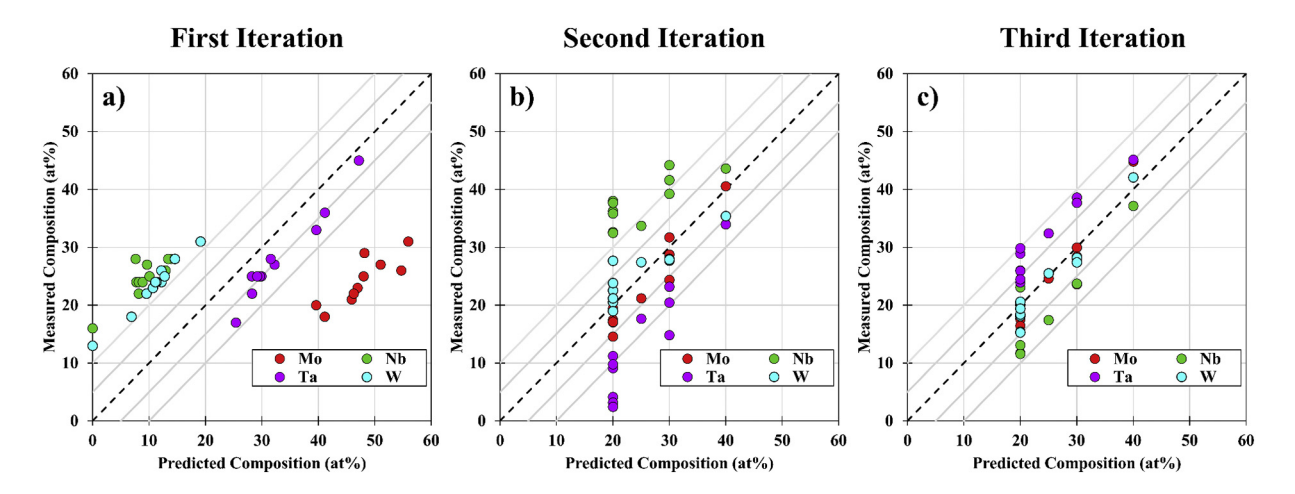


Fig. 4. Measured composition of additively manufactured sample stubs versus the predicted composition for the a) first, b) second, and c) third printing iterations. The black dashed line denotes a 1:1 prediction while the light gray lines adjacent are \pm 5-at% and \pm 10-at% contours.

calculated proactively and used for printing the second iteration. Comparison of the measured compositions and the predicted compositions for the second iteration are shown in Fig. 4b. Here the data is organized into columns (a direct result of the targeted compositions) and improvements have been made over the first iteration: Mo and W are within ± 10 at.% for all targeted compositions and while Nb is overrepresented and Ta is underrepresented, there are several compositions which also fall within the ± 10 at.% range.

3.1.3. Third iteration

While the second iteration provided better predictability over using powder flow rate measurements alone (compare Fig. 4a and b), there is still substantial variation in the actual final compositions with respect to their predictions. To further improve the predictive capability, for the third iteration the previous experimentally determined mass flow rate coefficients (α_i and β_i) in addition to the retention rate (R_i) were used as fitting parameters; additionally, the constraint of $0 \le R_i \le 1$ was removed. To refine these fitting parameters, the least-squares fit of Eq. (4) was then repeated using input RPMs and measured compositions from the second iteration. With the fitting parameters redefined, RPMs necessary to produce the same target compositions from the second iteration were calculated and used for printing the third iteration.

Following the same procedure as before, the actual compositions of each sample stub were measured using EDS and compared to the predicted compositions, the results of which are shown in Fig. 4c. Here a marked improvement is seen in the predictability: both Mo and W are within ± 5 at.% for all targeted compositions and both Nb and Ta are within ± 10 at.% for all targeted compositions. The RPMs used for each printed stub, as well as the predicted and measured chemical compositions, are given explicitly in Table A1.

3.2. Surface morphology and chemical analysis

The as-fabricated top surface of each sample stub was imaged using SEM. Both the as-fabricated top surface and the polished top surface of a

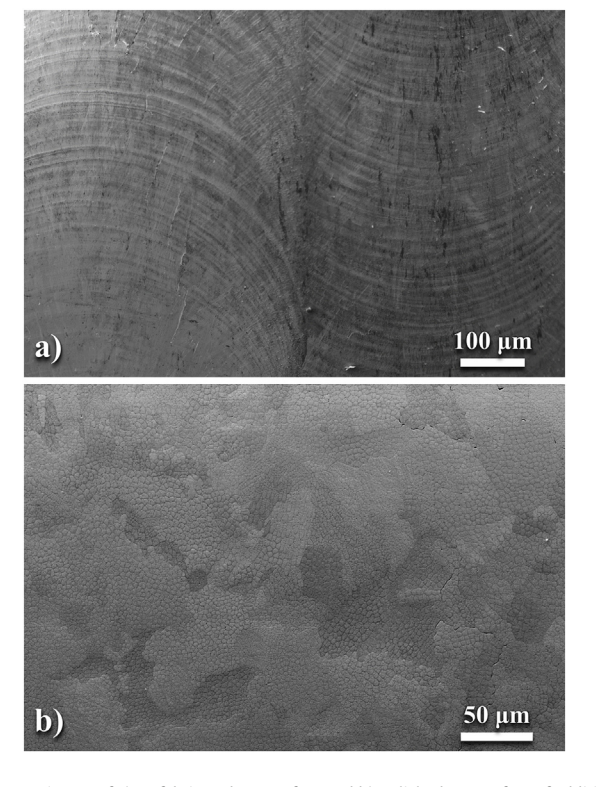


Fig. 5. SEM image of a) as-fabricated top surface and b) polished top surface of additively manufactured nearly equimolar MoNbTaW sample. Sample BR3 in Table A1.

sample stub near the equimolar MoNbTaW composition are shown in Fig. 5a and b, respectively. The as-fabricated surface morphology exhibits a weld-like pattern that shares the same dimensions and directionality as the remelting raster pattern. After mechanical polishing, the grain structure is revealed and exhibits a cellular solidification structure within the grains. Additionally, most of the sample stubs exhibited minor intergranular cracking, likely caused by the thermal stresses from cooling from temperatures >3500 °C (necessary to melt tungsten) to room temperature in seconds. Importantly, little to no retained unmelted powder was observed in the remelted region on the top surface of the sample which validates the necessity of laser remelting.

In addition to performing broad EDS line scans to determine the average composition of each sample, EDS chemical mapping was performed at higher magnification to assess the micro-segregation of alloying elements. Fig. 6 shows the elemental distribution of both the additively manufactured and arc-melted equimolar MoNbTaW produced for comparison.

Generally speaking, from thermodynamics of solidification, segregation of solute elements will occur as a result of a difference in solubility of these elements in the liquid and solid phases. While thermodynamically driven, the length scale over which this occurs is dictated by solidification kinetics and specifically the degree of undercooling which can be related to the cooling rate of the system [33]. As may be expected, the length scale of the cellular structure in the additively manufactured material is much finer than the dendritic structure in the arc-melted material which is indicative of a faster cooling rate in the case of the additively manufactured material. Both the additively manufactured and arc-melted equimolar MoNbTaW HEA exhibited similar differences in chemical composition between the inter- and intra- cellular/dendritic regions of the as-solidified microstructure. These local compositions, measured by EDS, are given in Table 1 and are in good agreement with measurements on arc-melted MoNbTaW from literature [34].

The length scale of the chemical segregation is particularly relevant when seeking to homogenize the material through heat treatment. Using $x \approx 2\sqrt{D \cdot t}$ as an estimate for the diffusion length and assuming the interdiffusion coefficients of the two alloys are comparable, the difference in time required to homogenize each alloy can be estimated. From inspection of Fig. 6, the interdendritic spacing of the arc-melted material is estimated to be ~4–5 times greater than the intercellular spacing in the additively manufactured material. This would suggest that the arc-melted material would take ~16–25 times *longer* to homogenize than the additively manufactured material.

3.3. Phase characterization

X-ray diffraction (XRD) was performed on each sample stub from the arrays, the resulting patterns of which are shown in Fig. 7 with intensities normalized to the first major peak. Each pattern consists of purely BCC peaks without additional signals from otherwise forbidden reflections which would be indicative of ordered phases; as a result, each composition was determined to be a disordered BCC solid solution. Of note is the variation in relative intensity of the diffraction peaks within a given diffraction pattern which may be caused by texturing or the relatively large grains seen in Fig. 5, leading to only a small number of grains being interrogated. Indeed, it is not uncommon for additive manufacturing techniques to produce a textured structure or large grains when depositing using high energy densities [35].

From the XRD patterns, lattice parameters of each alloy were calculated by performing a Nelson-Riley regression on the lattice parameters calculated from each reflection within a pattern [28]. Additionally, since each composition forms a solid solution, the expected lattice parameter can be calculated from a weighted average of the constituent elements (Vegard's law) which has been performed and listed for each sample alongside the measured lattice parameter in Table A1. As may be expected, ~95% of the measured lattice parameters were within 0.5% of

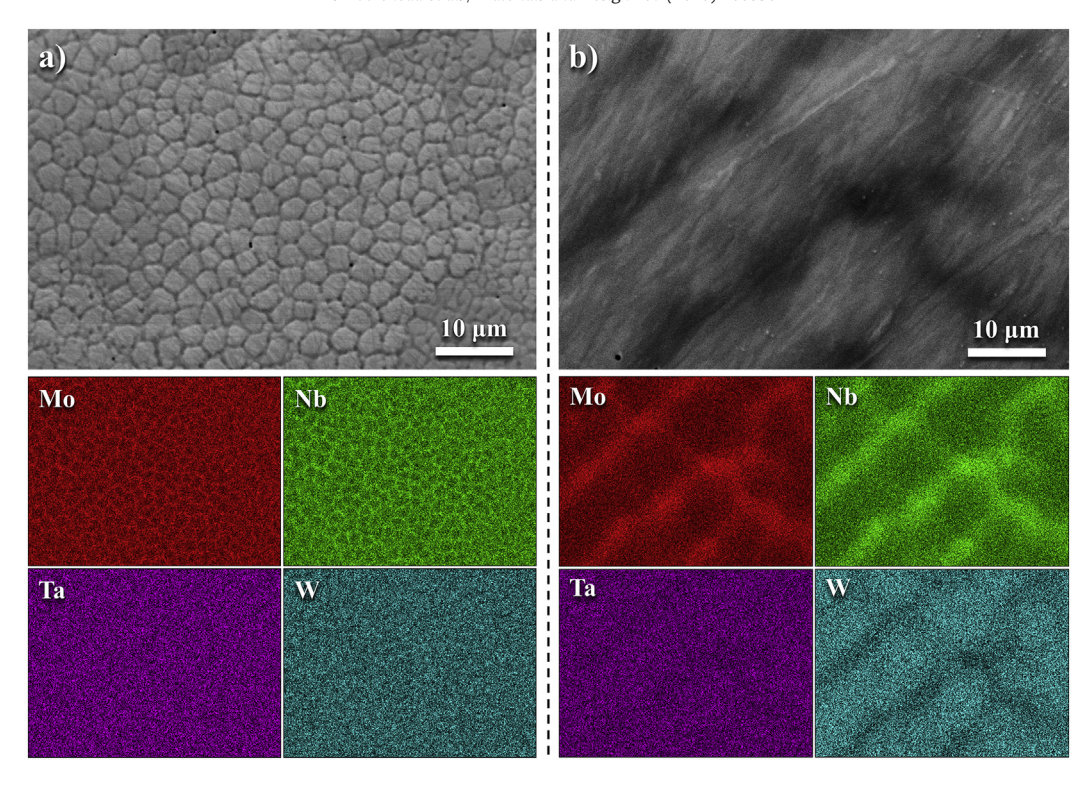


Fig. 6. SEM image and EDS chemical mapping of equimolar MoNbTaW produced through a) additive manufacturing (sample BR3 in Appendix) and b) are melting. Note: the images are taken at the same magnification to illustrate the extent of chemical segregation.

the lattice parameters predicted using Vegard's law - the measured lattice parameter of only one sample was found to deviate >1% from Vegard's law.

While every printed sample was experimentally found to consist of a single disordered BCC structure, as expected from high-temperature CALPHAD calculations, it is not known whether this is the thermodynamically stable phase for each composition at lower temperatures, as only the equimolar MoNbTaW HEA has been studied extensively in literature [22-25]. To elucidate this, high-throughput CALPHAD calculations were performed over the Mo-Nb-Ta-W composition space using PanDat™, spanning all composition bound by 5 at.% to 50 at.% for each element, with a step size of 5 at.%, to determine the stable phases at 300 °C. The resultant stable-phase predictions for each composition were used to produce a quaternary phase diagram, shown in Fig. 8 with the compositions of the additively manufactured samples superimposed. Here, it can be seen that Nb acts to stabilize the single disordered BCC phase while Ta acts to destabilize the single disordered BCC phase, leading to phase separation and formation of an ordered BCC secondary phase. The vast majority of the alloys produced as part of this study are predicted to remain thermodynamically stable as a single disordered BCC at 300 °C, however, some Ta-rich and Nb-poor compositions are predicted to form second phases. Under normal conditions, the formation of these second phases would not be expected due to

Table 1Comparison of local chemical composition measured by EDS of equimolar MoNbTaW synthesized by additive manufacturing and arc melting.

Region	Additively m	nanufactured	Arc melted						
	Intracellular	Intercellular	Intradendritic	Interdendritic					
Mo (at.%)	23 ± 2	26 ± 2	22 ± 2	25 ± 2					
Nb (at.%)	23 ± 2	31 ± 2	23 ± 2	32 ± 2					
Ta (at.%)	25 ± 2	21 ± 2	26 ± 3	24 ± 3					
W (at.%)	29 ± 3	23 ± 3	29 ± 3	19 ± 3					

the slow diffusivity of refractory metals at lower temperatures, however, in a kinetically driven system (such as under irradiation) it may be possible for such phases to form which could potentially lead to changes in material properties such as hardening and embrittlement. It is noted that results from CALPHAD calculations of refractory HEA compositions at low temperatures must be used conscientiously, as many of the chemical potentials used for these calculations are the result of extrapolations from higher temperatures and more dilute concentrations [36], which can lead to greater uncertainties – thus necessitating experimental validation through long-term aging experiments.

4. Discussion

4.1. Printing considerations

Although visual inspection of the as-built materials revealed cracking along the build-plate/sample interface visible in Fig. 3, the samples remained well adhered to the build plate. Such cracking is to be expected given the thermal stresses produced during additive manufacturing especially with the difference in coefficient of thermal expansion (CTE) between the stainless-steel build plate and the refractory samples; the CTE of 316 stainless steel is $2\text{-}3\times$ greater than that of Mo, Nb, Ta, and W at room temperature [37]. Future printing campaigns will attempt to match the thermo-mechanical properties of printed material with build-plate material selection to minimize thermal stresses where possible, for example, by using pure Mo, Nb, Ta, or W build plates when printing with these elements.

A common challenge encountered when printing with elemental powders is the incorporation of unmelted powder, and overall lack of chemical homogeneity in the final product [32,38–40]. This problem can become more pronounced when working with high-melting-point materials as was observed in preliminary experiments in the Mo-Nb-Ta-W system as part of this study. Previous studies have combatted this problem by using either pre-alloyed or pre-mixed powder

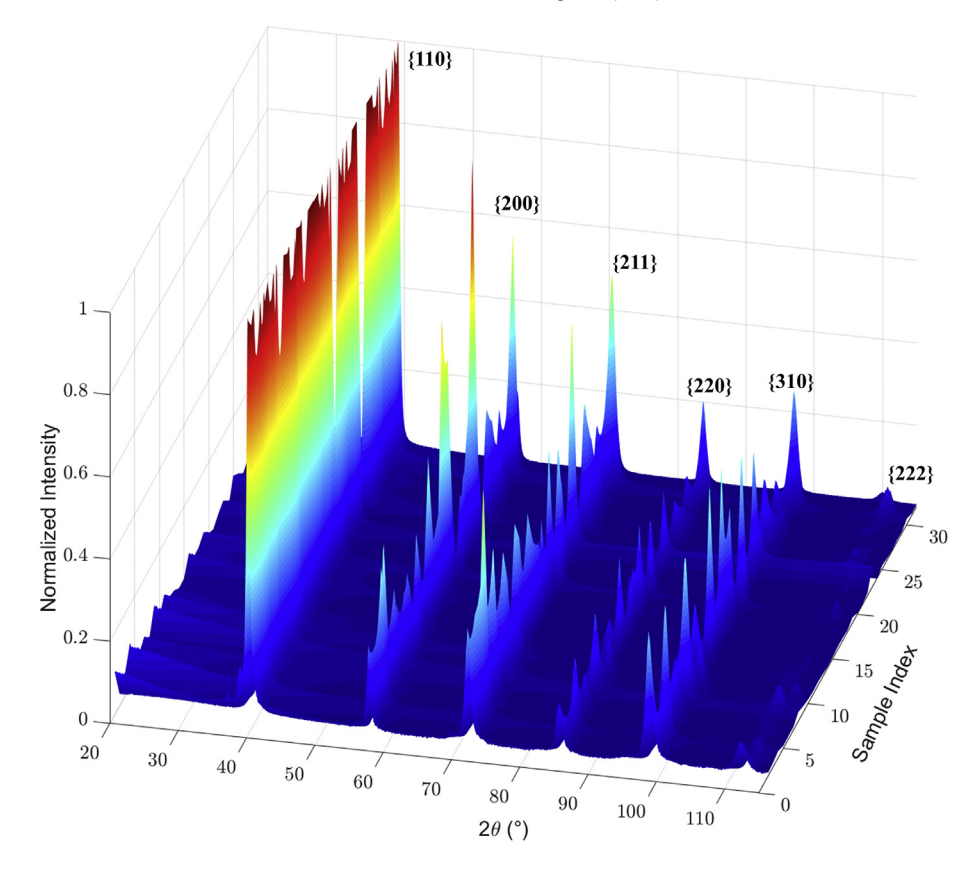


Fig. 7. Composite image of XRD patterns from the 31 sample stubs analyzed. All samples appear to exhibit only a single-phase, disordered BCC crystal structure.

[41–43] or by introducing remelting passes during printing [32,44,45]. Unfortunately, the use of pre-alloyed or pre-mixed powder immediately limits the ability to rapidly explore different alloy compositions, thus in this work laser remelting was used to preserve this capability.

Unmelted powder retention was first minimized in this work by adjusting printing parameters such as lowering powder flow rates, increasing laser power, lowering scan speed, and decreasing hatch spacing,

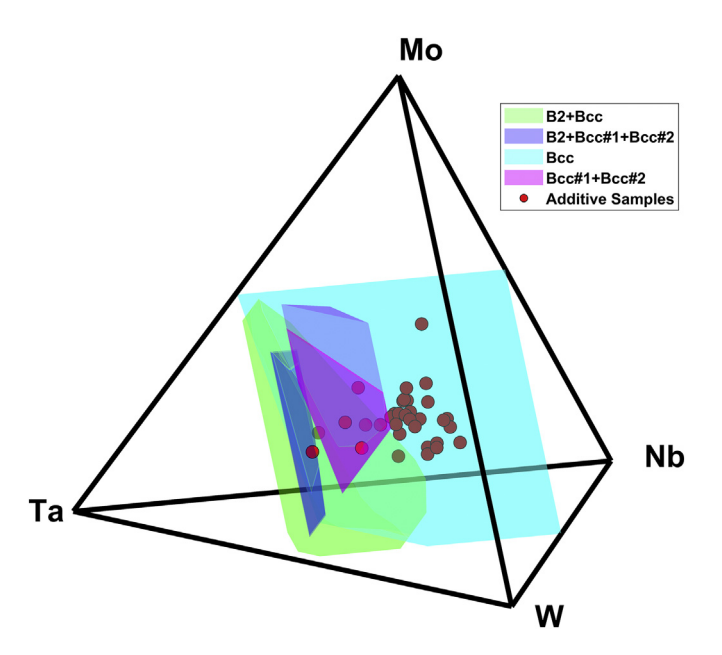


Fig. 8. Quaternary phase diagram of Mo-Nb-Ta-W system at 300 $^{\circ}\text{C}$ as calculated using high-throughput CALPHAD calculations.

specifically to increase the amount of energy deposited per unit mass of powder and the time each location remains molten during printing. Nevertheless, unmelted powder was still observed to the extent that laser remelting was still deemed necessary. In the interest of synthesis time, only a single laser remelting pass at the end of the build was used to produce a homogeneous layer. This was motivated by future materials testing, such as ion irradiation, corrosion, and micromechanical testing, performed in the near-surface regions of the material. On the other hand, this remelting technique could be applied throughout the build process to ensure a larger extent of chemical homogeneity in the build depth. Sample stubs of the selected alloys were still required to be built several layers high to avoid artifacts from the interaction region with the substrate such as interdiffusion of substrate material into the final part.

When performing in situ alloying of elemental powders through additive manufacturing, it is also important to bear in mind that the composition of the powder being flown through the system may not necessarily be the composition of the final additively manufactured alloy. For example, to achieve the near-equimolar MoNbTaW composition in sample R8.1 (actual composition Mo₂₃Nb₂₄Ta₂₅W₂₈), the composition of the powder used was approximately 47 at.% Mo, 9 at.% Nb, 30 at.% Ta, and 14 at.% W. Previous work with this system has related this discrepancy to the melting point and vapor pressure of the different elements [32]. However, since numerous other factors including powder oxide thickness [46], powder size distribution [47], powder morphology [48], etc. can also affect the melting and spatial distribution of elements in the final part, optimization through iterative trial prints appears much more tractable to achieve desired compositions in lieu of exhaustive bottom-up modeling efforts.

4.2. High-throughput implications

In addition to greatly expanding the variety of geometries that can be fabricated as compared to conventional metallurgy methods, additive manufacturing is similarly paving the way for alloy exploration. Since the number of possible alloy compositions increases dramatically with each additional constituent, and even more so by varying the concentration of each element in a system, most alloy development has occurred near to a singular base element, with few alloying additions. Thus, a vast space of potential alloys exists relatively unexplored, with high-entropy alloys residing at the heart of this new frontier.

The experiments presented herein have demonstrated how in situ alloying through additive manufacturing can be used to explore the HEA alloy space in a high-throughput manner. Using arc melting as a representative for conventional alloy synthesis techniques, the time savings of using in situ alloying through additive manufacturing for materials synthesis can be estimated semi-quantitatively with this study to be approximately one order of magnitude. Moreover, when considering the time necessary to homogenize arc-melted and additively manufactured materials through heat treatment, as shown in Section 3.2, the total time savings increase to over two orders of magnitude when using in situ alloying. For the application of ion irradiation, corrosion, and micromechanical testing specifically, there is an additional time savings gained since all samples can be tested simultaneously without having to load and unload each sample one at a time. Similarly, the time required to polish each sample to a surface roughness acceptable per ASTM standard [49], is likely far greater than would be necessary to polish a sample array on a sin-

High-throughput alloy development, however, requires additional aspects beyond materials synthesis, including characterization and modeling, and in order to achieve a comprehensive understanding of the material in question, all three are needed. It is thus critical to match high-throughput alloy processing rates for both fabrication and property characterization methods, as well as incorporate a highthroughput computational effort. Alongside the production of combinatorial thin films [11–14], additive manufacturing is one of the few synthesis methods versatile and fast enough to enable all three aspects to function synergistically in a high-throughput manner. Moreover, additive manufacturing affords many of the same flexibilities of combinatorial thin film synthesis while being able to produce bulk quantities of material (i.e. millimeters vs. micrometers of usable material) and can be readily scaled to produce larger volumes of material and different sample geometries as needed - a capability not available when using other high-throughput synthesis techniques.

The high-throughput synthesis and characterization methods employed in the work have also been used synergistically with CALPHAD modeling, via the software PanDat™, to assess the phase stability for the compositions printed from the Mo-Nb-Ta-W system. While modeling for this work was performed post facto, this need not be the case. Indeed, with the use of additive manufacturing, coarse modeling over large composition spaces could first be performed to determine regions of interest which could then be rapidly printed and characterized in a near-automatic fashion. In addition to microstructural characterization such as SEM, EDS, and XRD, other testing can be performed in a similar fashion such as resistivity measurements, micromechanical testing, and profilometry [50].

5. Conclusions and future work

In this work, high-throughput materials synthesis was combined with characterization and modeling techniques to form the framework for an accelerated approach toward alloy development using arrays of high-entropy alloys in the Mo-Nb-Ta-W system produced by in situ alloying of elemental powders through additive manufacturing. Use of separate elemental feedstock powders enabled the selection of any linear combination of the four elements, thus forming the basis for high-throughput alloy exploration and synthesis. Three printing iterations were performed to improve the predictive capabilities of the final sample compositions produced. By the third iteration, targeted

compositions could be printed within ± 5 at.% for Mo and W and within ± 10 at.% for Nb and Ta. Sample stubs produced were subsequently characterized using SEM, EDS, and XRD; all samples were found to be chemically homogeneous with minimal inclusions of unmelted powder and exhibit a single disordered BCC crystal structure. All characterization was performed non-destructively with samples remaining on the build plate, enabling future high-throughput testing to be performed using the same build plate. Additionally, the coupling of highthroughput synthesis and characterization techniques with highthroughput modeling was demonstrated using CALPHAD calculations via PanDat™ to predict the equilibrium phases of each printed alloy composition at 300 °C. While nearly every composition printed was predicted to remain a single disordered BCC crystal structure at 300 °C, certain Ta-rich and Nb-poor compositions were predicted to form second phases - however, the slow diffusivity of refractory metals at this temperature would likely inhibit their formation in practice.

CRediT authorship contribution statement

Michael Moorehead: Conceptualization, Methodology, Software, Validation, Formal analysis, Investigation, Data curation, Writing - original draft, Writing - review & editing, Visualization.Kaila Bertsch: Conceptualization, Investigation, Writing - review & editing. Michael Niezgoda: Methodology, Software, Investigation, Data curation. Calvin Parkin: Conceptualization, Formal analysis, Investigation. Mohamed Elbakhshwan: Conceptualization, Formal analysis, Investigation, Writing - review & editing, Supervision. Kumar Sridharan: Conceptualization, Writing - review & editing, Supervision. Chuan Zhang: Conceptualization, Methodology, Software, Formal analysis, Writing - original draft, Writing - review & editing. Dan Thoma: Conceptualization, Methodology, Resources, Writing - original draft, Writing - review & editing, Supervision, Funding acquisition. Adrien Couet: Conceptualization, Methodology, Resources, Writing - original draft, Writing - review & editing, Supervision, Funding acquisition.

Declaration of competing interest

The authors declare that they have no known competing financial interests or personal relationships that could have appeared to influence the work reported in this paper.

Acknowledgements

This research is being performed using funding received from the DOE Office of Nuclear Energy's Nuclear Energy University Program (DE-NE0008678). This research was funded in part by a fellowship program sponsored by the Nuclear Regulatory Commission (NRC). Additive manufacturing work using the LENS MR-7 was made possible through funding from the Grainger Institute for Engineering and NSF DMREF award #1728933. The authors gratefully acknowledge use of facilities and instrumentation at the UW-Madison Wisconsin Centers for Nanoscale Technology (wcnt.wisc.edu) partially supported by the NSF through the University of Wisconsin-Madison Materials Research Science and Engineering Center (DMR-1720415). The authors would also like to acknowledge HC Starck and ARPA-E for their support.

Additionally, the authors would like to acknowledge the team of undergraduate students who have contributed to this work including (alphabetically): Amy Lossen, Jake Quincey, Matthew Weinstein, and laden Umana.

Data availability

The raw/processed data required to reproduce these findings cannot be shared at this time as the data also forms part of an ongoing study.

Appendix A

Table A1
Input RPMs, estimated incoming powder composition, printed sample composition measured via EDS, lattice parameter measured via XRD, and predicted lattice parameter from Vegard's law for each of the printed samples included in this study. Note the difference between input and actual powder hopper RPM, as this likely changes between systems and software versions. R(X).1 samples are from the first iteration, R(X).2 samples are from the second iteration, and BR(X) samples are from the third iteration. Also note that compositional predictions from the first iteration are increasingly prone to error at lower RPMs (e.g. sample 8D.1) due to scatter in the mass flow rate measurements at low flow rates.

Sample index	Sample name	Input powder hopper RPM			Actual powder hopper RPM			Estimated powder composition (at.%)			Measured sample composition (at.%)				Lattice parameter (Angstroms)				
		Mo	Nb	Ta	W	Мо	Nb	Ta	W	Мо	Nb	Ta	W	Мо	Nb	Ta	W	Measured	Vegard's law
1	R1.1	0.3	2.1	-0.4	2.2	2.7	1.7	2.2	1.8	46	10	32	12	21	27	27	24	3.218	3.203
2	R2.1	0.0	2.0	-0.4	2.8	2.5	1.6	2.2	2.2	41	8	32	19	18	22	28	31	3.216	3.198
3	R3.1	1.0	2.0	-0.4	2.2	3.3	1.6	2.2	1.8	51	8	30	11	27	24	25	24	3.214	3.227
4	R4.1	0.0	2.0	0.5	2.0	2.5	1.6	2.9	1.6	41	8	41	10	18	24	36	22	3.228	3.243
5	R5.1	1.0	2.5	-0.4	2.2	3.3	2.0	2.2	1.8	48	13	28	11	29	26	22	23	3.216	3.225
6	R6.1	0.0	2.5	0.5	1.8	2.5	2.0	2.9	1.4	40	14	40	7	20	28	33	18	3.233	3.213
7	R7.1	1.5	2.0	-0.8	2.2	3.7	1.6	1.9	1.8	56	8	25	11	31	28	17	24	3.214	3.221
8	R8.1	0.7	2.1	-0.4	2.5	3.1	1.7	2.2	2.0	47	9	30	15	23	24	25	28	3.220	3.227
9	R9.1	1.2	1.2	1.2	1.2	3.5	1.0	3.5	1.0	54	0	46	0	26	16	45	13	3.231	3.243
10	R10.1	0.7	2.5	-0.5	2.3	3.1	2.0	2.1	1.8	46	13	28	12	22	28	25	26	3.218	3.265
11	R1.2	-0.3	1.9	-0.2	2.4	2.3	1.5	2.3	1.9	40	8	36	15	19	38	15	28	3.218	3.233
12	R2.2	0.0	2.3	-1.1	2.5	2.5	1.8	1.6	2.0	44	13	26	16	21	42	9	28	3.224	3.230
13	R3.2	0.9	1.9	-1.4	2.3	3.2	1.5	1.4	1.8	56	7	22	14	32	36	4	28	3.209	3.214
14	R4.2	-0.2	2.3	-0.2	2.0	2.3	1.8	2.3	1.6	41	12	37	10	17	29	23	21	3.246	3.247
15	R5.2	0.6	1.9	-0.6	1.9	3.0	1.5	2.0	1.5	53	7	32	9	24	33	20	23	3.226	3.233
16	R6.2	0.9	2.2	-1.4	1.9	3.2	1.8	1.4	1.5	57	11	23	9	29	44	3	24	3.219	3.224
17	R7.2	1.6	1.8	-1.6	1.8	3.8	1.4	1.2	1.4	66	7	20	8	41	36	2	21	3.204	3.210
18	R8.2	0.0	2.7	-1.0	2.1	2.5	2.2	1.7	1.7	44	18	27	11	17	44	11	28	3.237	3.236
19	R9.2	-0.5	1.9	0.6	1.9	2.1	1.5	3.0	1.5	38	8	45	9	15	32	34	19	3.251	3.253
20	R10.2	-0.1	2.0	-1.1	2.9	2.4	1.6	1.6	2.3	43	9	26	22	17	38	10	35	3.217	3.226
21	R11.2	0.3	2.1	-0.8	2.2	2.7	1.7	1.9	1.8	49	10	29	12	21	34	18	27	3.222	3.231
22	BR2	-0.2	1.2	-0.6	2.2	2.3	1.0	2.0	1.8	25	28	18	29	18	28	26	28	3.228	3.235
23	BR3	0.5	0.5	-0.6	2.2	2.9	0.4	2.0	1.8	36	18	17	28	24	23	26	27	3.220	3.227
24	BR4	-0.2	1.2	0.0	1.5	2.3	1.0	2.5	1.2	25	28	27	20	18	24	39	20	3.231	3.247
25	BR5	0.6	0.5	-0.1	1.5	3.0	0.4	2.4	1.2	37	18	26	19	30	12	38	21	3.217	3.227
26	BR6	0.6	1.1	-0.6	1.4	3.0	0.9	2.0	1.1	37	27	17	19	28	27	29	15	3.236	3.236
27	BR7	1.3	0.5	-0.7	1.4	3.5	0.4	1.9	1.1	47	17	17	18	45	13	24	18	3.198	3.207
28	BR8	-0.2	1.8	-0.6	1.5	2.3	1.4	2.0	1.2	25	37	18	20	20	37	24	18	3.233	3.245
29	BR9	-0.2	0.6	0.6	1.5	2.3	0.5	3.0	1.2	25	19	36	20	20	15	45	19	3.239	3.244
30	BR10	-0.2	0.5	-0.6	3.0	2.3	0.4	2.0	2.4	25	18	18	39	16	12	30	42	3.208	3.219
31	BR11	0.2	0.8	-0.3	1.8	2.7	0.6	2.3	1.4	31	23	22	24	25	17	32	26	3.218	3.228

Appendix B. Supplementary data

Supplementary data to this article can be found online at https://doi.org/10.1016/j.matdes.2019.108358.

References

- J.W. Yeh, S.K. Chen, S.J. Lin, J.Y. Gan, T.S. Chin, T.T. Shun, C.H. Tsau, S.Y. Chang, Nanostructured high-entropy alloys with multiple principal elements: novel alloy design concepts and outcomes, Adv. Eng. Mater. 6 (5) (2004) 299–303.
- [2] T. Yang, C. Li, S.J. Zinkle, S. Zhao, H. Bei, Y. Zhang, Irradiation responses and defect behavior of single-phase concentrated solid solution alloys, J. Mater. Res. 33 (19) (2018) 2077, 2001.
- [3] O.N. Senkov, D.B. Miracle, K.J. Chaput, J.-P. Couzinie, Development and exploration of refractory high entropy alloys—a review, J. Mater. Res. 33 (19) (2018) 3092–3128.
- [4] Y. Shi, B. Yang, P. Liaw, Corrosion-resistant high-entropy alloys: a review, Metals 7 (2) (2017) 43.
- [5] Y. Zhang, Preparation methods of high-entropy materials, in: Y. Zhang (Ed.), High-Entropy Materials: A Brief Introduction, Springer Singapore, Singapore 2019, pp. 65–75.
- [6] S. Riva, S.G.R. Brown, N.P. Lavery, A. Tudball, K.V. Yusenko, Spark plasma sintering of high entropy alloys, in: P. Cavaliere (Ed.), Spark Plasma Sintering of Materials: Advances in Processing and Applications, Springer International Publishing, Cham 2019, pp. 517–538.
- [7] M. Vaidya, G.M. Muralikrishna, B.S. Murty, High-entropy alloys by mechanical alloying: a review, J. Mater. Res. 34 (5) (2019) 664–686.
- [8] W. Li, P. Liu, P.K. Liaw, Microstructures and properties of high-entropy alloy films and coatings: a review, Materials Research Letters 6 (4) (2018) 199–229.
- [9] P. Wilson, R. Field, M. Kaufman, The use of diffusion multiples to examine the compositional dependence of phase stability and hardness of the Co-Cr-Fe-Mn-Ni high entropy alloy system, Intermetallics 75 (2016) 15–24.
- [10] J.C. Zhao, X. Zheng, D.G. Cahill, High-throughput diffusion multiples, Mater. Today 8 (10) (2005) 28–37.

- [11] A. Ludwig, R. Zarnetta, S. Hamann, A. Savan, S. Thienhaus, Development of multifunctional thin films using high-throughput experimentation methods, Int. J. Mater. Res. 99 (10) (2008) 1144–1149.
- [12] P.J.S. Buenconsejo, A. Siegel, A. Savan, S. Thienhaus, A. Ludwig, Preparation of 24 ternary thin film materials libraries on a single substrate in one experiment for irreversible high-throughput studies, Am. Chem. Soc. 14 (1) (2011) 25–30.
- [13] T. Gebhardt, D. Music, T. Takahashi, J. Schneider, Combinatorial thin film materials science: from alloy discovery and optimization to alloy design, Thin Solid Films 520 (17) (2012) 5491–5499.
- [14] D. König, J. Pfetzing-Micklich, J. Frenzel, A. Ludwig, Investigation of ternary subsystems of superalloys by thin-film combinatorial synthesis and high-throughput analysis, MATEC Web of Conferences 14 (2014), 18002.
- [15] T. Borkar, B. Gwalani, D. Choudhuri, C.V. Mikler, C.J. Yannetta, X. Chen, R.V. Ramanujan, M.J. Styles, M.A. Gibson, R. Banerjee, A combinatorial assessment of AlxCrCuFeNi2 (0 < x < 1.5) complex concentrated alloys: microstructure, microhardness, and magnetic properties, Acta Mater. 116 (2016) 63–76.</p>
- [16] D.C. Hofmann, J. Kolodziejska, S. Roberts, R. Otis, R.P. Dillon, J.-O. Suh, Z.-K. Liu, J.-P. Borgonia, Compositionally graded metals: a new frontier of additive manufacturing, J. Mater. Res. 29 (17) (2014) 1899–1910.
- [17] P. Tsai, K.M. Flores, High-throughput discovery and characterization of multicomponent bulk metallic glass alloys, Acta Mater. 120 (2016) 426–434.
- [18] R.X. Li, P.K. Liaw, Y. Zhang, Synthesis of AlxCoCrFeNi high-entropy alloys by high-gravity combustion from oxides, Mater. Sci. Eng. A 707 (2017) 668–673.
- [19] Y. Xu, Y. Bu, J. Liu, H. Wang, In-situ high throughput synthesis of high-entropy alloys, Scr. Mater. 160 (2019) 44–47.
- [20] M. Li, J. Gazquez, A. Borisevich, R. Mishra, K.M. Flores, Evaluation of microstructure and mechanical property variations in AlxCoCrFeNi high entropy alloys produced by a high-throughput laser deposition method, Intermetallics 95 (2018) 110–118.
- [21] D.J. Thoma, G.K. Lewis, R.B. Nemec, Solidification Behavior during Directed Light Fabrication, United States 1995 7.
- 22] O. Senkov, G. Wilks, J. Scott, D. Miracle, Mechanical properties of Nb25Mo25Ta25W25 and V20Nb20Mo20Ta20W20 refractory high entropy alloys, Intermetallics 19 (5) (2011) 697–706.
- [23] Y. Zou, S. Maiti, W. Steurer, R. Spolenak, Size-Dependent Plasticity in an Nb25Mo25Ta25W25 Refractory High-Entropy Alloy, 2014.

- [24] F. Körmann, M. Sluiter, Interplay between lattice distortions, vibrations and phase stability in NbMoTaW high entropy alloys, Entropy 18 (8) (2016) 403.
- [25] F. Körmann, A.V. Ruban, M.H.F. Sluiter, Long-ranged interactions in bcc NbMoTaW high-entropy alloys, Materials Research Letters 5 (1) (2017) 35–40.
- [26] J.P. Oliveira, T.G. Santos, R.M. Miranda, Revisiting fundamental welding concepts to improve additive manufacturing: from theory to practice, Prog. Mater. Sci. 107 (2020), 100590.
- [27] N.T. Aboulkhair, N.M. Everitt, I. Ashcroft, C. Tuck, Reducing porosity in AlSi10Mg parts processed by selective laser melting, Additive Manufacturing 1–4 (2014) 77–86.
- [28] J.B. Nelson, D.P. Riley, An experimental investigation of extrapolation methods in the derivation of accurate unit-cell dimensions of crystals, Proc. Phys. Soc. 57 (3) (1945) 160
- [29] L. Kaufman, H. Bernstein, Computer Calculation of Phase Diagrams With Special Reference to Refractory Metals, Academic Press Inc, United States, 1970.
- [30] U.R. Kattner, The CALPHAD method and its role in material and process development, Tecnol Metal Mater Min 13 (1) (2016) 3–15.
- [31] PanDat, Thermodynamic Calculations and Kinetic Simulations, CompuTherm LLC, 2019
- [32] H. Dobbelstein, M. Thiele, E.L. Gurevich, E. P.G., A. Ostendorf, Direct metal deposition of refractory high entropy alloy MoNbTaW, Phys. Procedia 83 (2016) 624–633.
- [33] D.A. Porter, K.E. Easterling, M.Y. Sherif, Phase Transformations in Metals and Alloys, 2009.
- [34] O. Senkov, G. Wilks, D. Miracle, C. Chuang, P. Liaw, Refractory high-entropy alloys, Intermetallics 18 (9) (2010) 1758–1765.
- [35] L.L. Parimi, R.G. A, D. Clark, M.M. Attallah, Microstructural and texture development in direct laser fabricated IN718, Mater. Charact. 89 (2014) 102–111.
- [36] A. Raturi, J. Aditya C, N.P. Gurao, K. Biswas, ICME approach to explore equiatomic and non-equiatomic single phase BCC refractory high entropy alloys, J. Alloys Compd. 806 (2019) 587–595.
- [37] R.J. Corruccini, J.J. Gniewek, Thermal Expansion of Technical Solids at Low Temperatures; A Compilation From the Literature, U.S. Dept. of Commerce, National Bureau of Standards, Washington, 1961.
- [38] L. Li, W.U.H. Syed, A.J. Pinkerton, Rapid additive manufacturing of functionally graded structures using simultaneous wire and powder laser deposition, Virtual and Physical Prototyping 1 (4) (2006) 217–225.
- [39] H. Taheri, M.R.B.M. Shoaib, L.W. Koester, T.A. Bigelow, P.C. Collins, L.J. Bond, Powder-based additive manufacturing a review of types of defects, generation

- mechanisms, detection, property evaluation and metrology, International Journal of Additive and Subtractive Materials Manufacturing 1 (2) (2017) 172–209
- [40] T. DebRoy, H.L. Wei, J.S. Zuback, T. Mukherjee, J.W. Elmer, J.O. Milewski, A.M. Beese, A. Wilson-Heid, A. De, W. Zhang, Additive manufacturing of metallic components – process, structure and properties, Prog. Mater. Sci. 92 (2018) 112–224.
- [41] A. Piglione, B. Dovgyy, C. Liu, C.M. Gourlay, P.A. Hooper, P. M.S., Printability and microstructure of the CoCrFeMnNi high-entropy alloy fabricated by laser powder bed fusion, Mater. Lett. 224 (2018) 22–25.
- [42] S. Xiang, H. Luan, J. Wu, K.-F. Yao, J. Li, X. Liu, Y. Tian, W. Mao, H. Bai, G. Le, Q. Li, Microstructures and mechanical properties of CrMnFeCoNi high entropy alloys fabricated using laser metal deposition technique, J. Alloys Compd. 773 (2019) 387–392.
- [43] J. Joseph, T. Jarvis, X. Wu, N. Stanford, P. Hodgson, D.M. Fabijanic, Comparative study of the microstructures and mechanical properties of direct laser fabricated and arcmelted AlxCoCrFeNi high entropy alloys, Mater. Sci. Eng. A 633 (2015) 184–193.
- [44] H. Dobbelstein, E.L. Gurevich, E.P. George, A. Ostendorf, G. Laplanche, Laser metal deposition of a refractory TiZrNbHfTa high-entropy alloy, Additive Manufacturing 24 (2018) 386–390.
- [45] H. Dobbelstein, E.L. Gurevich, E.P. George, A. Ostendorf, G. Laplanche, Laser metal deposition of compositionally graded TiZrNbTa refractory high-entropy alloys using elemental powder blends, Additive Manufacturing 25 (2019) 252–262, https://doi.org/10.1016/j.addma.2018.10.042(January 2019).
- [46] Y.H. Zhou, Z.H. Zhang, Y.P. Wang, G. Liu, S.Y. Zhou, Y.L. Li, J. Shen, M. Yan, Selective laser melting of typical metallic materials: an effective process prediction model developed by energy absorption and consumption analysis, Additive Manufacturing 25 (2019) 204–217.
- [47] W. Li, L. Yan, X. Chen, J. Zhang, X. Zhang, F. Liou, Directed energy depositing a new Fe-Cr-Ni alloy with gradually changing composition with elemental powder mixes and particle size' effect in fabrication process, J. Mater. Process. Technol. 255 (2018) 96-104.
- [48] A.B. Spierings, M. Voegtlin, T. Bauer, K. Wegener, Powder flowability characterisation methodology for powder-bed-based metal additive manufacturing, Progress in Additive Manufacturing 1 (1) (2016) 9–20.
- [49] ASTM, Standard Practice for Investigating the Effects of Neutron Radiation Damage Using Charged-Particle Irradiation, 2018.
- [50] R. Löbel, S. Thienhaus, A. Savan, A. Ludwig, Combinatorial fabrication and highthroughput characterization of a Ti–Ni–Cu shape memory thin film composition spread, Mater. Sci. Eng. A 481–482 (2008) 151–155.